Photoionization of ground and excited states of Ca$^+$ and comparison along the isoelectronic sequence

A. M. Sossah,[*] H.-L. Zhou, and S. T. Manson

Department of Physics and Astronomy, Georgia State University. Atlanta, Georgia 30303, USA

Photoionization cross-section calculations are performed on the ground state ([Ne]$3s^23p^64s\,^2S^e_{1/2}$) and the first two excited states ([Ne]$3s^23p^63d\,^2D^e_{3/2}$ and [Ne]$3s^23p^63d\,^2D^e_{5/2}$) of Ca$^+$ ions for photon energies from threshold to 45.0 eV using the relativistic (Breit-Pauli) R-matrix method. The discrete Ca^{2+} orbitals are generated using the computer program AUTOSTRUCTURE; 30 configurations are included in the configuration-interaction calculation for the states of Ca^{2+}. The prominent $3p \rightarrow 3d$ giant resonances are analyzed and identified, and our results are compared with experimental results, and rather good agreement is found. Using results of our previous photoionization calculations on Sc^{2+} and Ti^{3+} ions, the strongest and broadest resonances in the photoionization cross section of those three ions (Ca$^+$, Sc^{2+}, and Ti^{3+}), in terms of width and oscillator strengths, are compared to show the evolution as a function of nuclear charge.

PACS number(s): 32.80.Fb, 32.80.Aa, 32.80.Zb

I. INTRODUCTION

In the study of photoionization of potassiumlike transition-metal ions [1,2] belonging to the iron group ($30 \geqslant Z \geqslant 21$), it is found that in the case of lower-Z ($22 \geqslant Z \geqslant 21$) ions (Sc^{2+} and Ti^{3+}), the cross-section spectra are dominated by the giant ($3p \rightarrow 3d$ excitation) resonances, while those of higher-Z ($30 \geqslant Z \geqslant 23$) ions (V^{4+}, Cr^{5+}, Mn^{6+}, Fe^{7+}, Co^{8+}, Ni^{9+}, Cu^{10+}, and Zn^{11+}) are dominated by the higher members of the ($3p^5nd$) $3d$ and ($3p^5n's$) $3d$ series of Rydberg resonances; the giant ($3p \rightarrow 3d$ excitation) resonances have moved below the ionization threshold [3,4]. The occurrence of giant resonances in transition-metal atoms and ions has been extensively investigated throughout the years [4–7], and it is shown that those particular resonances are also present in photoionization spectra of atomic Ca and its ions, but not in potassium [7,8]. Along the potassium isoelectronic sequence, experimental results [3,4] have shown that the alkaline-earth-metal ion Ca$^+$ and transition-metal ions Sc^{2+} and Ti^{3+} exhibited the same behavior in the $3p$ excitation region where the main features of their photoionization cross sections are those giant resonances, but there are no theoretical results yet to confirm these results. Note that the Ca$^+$ ions' ground- and excited-state electronic configurations are, respectively, [Ne]$3s^23p^64s\,^2S^e$ and [Ne]$3s^23p^63d\,^2D^e$, while for Sc^{2+} and Ti^{3+} ions they are [Ne]$3s^23p^63d\,^2D^e$ and [Ne]$3s^23p^64s\,^2S^e$. These electronic configurations demonstrate that Ca$^+$ along with Sc^{2+} and Ti^{3+} are at the nexus of the competition between the $4s$ and $3d$ orbitals, competition that is primarily driven by the antagonist effects produced by the net coulomb attraction from the nucleus and core electrons and the centrifugal barrier proportional to $l(l+1)$.

In this work we report on the study of the photoionization of ground- and excited-state Ca$^+$ ions and comparison along the isoelectronic sequence; our goal is to compare photoionization cross-section calculation results for Ca$^+$, Sc^{2+}, and Ti^{3+} ions. From our previous works [1,2], we have theoretical data on

Sc^{2+} and Ti^{3+} ions, therefore to attain our goal, we need to first perform photoionization cross-section calculations for Ca$^+$ in the ground and excited states. Ca$^+$ ions were the subject of several theoretical investigations in the last two decades; among them are photoionization cross-section calculations for the ground state [Ne]$3s^23p^64s\,^2S^e$ [9,10] and oscillator strength calculations including both ground [Ne]$3s^23p^64s\,^2S^e$ and excited [Ne]$3s^23p^63d\,^2D^e$ states [11,12]. On the experimental front, photoionization cross-section data for Ca$^+$ ions are available [4,13–16], and reveal discrepancies with the latest previous theoretical photoionization cross-section calculations [10]. We must add here that up to date, to the best of our knowledge, no theoretical photoionization cross-section calculations for Ca$^+$ including the excited (metastable) [Ne]$3s^23p^63d\,^2D^e$ state of this ion are found; they are limited to the ground state only [9,10].

The photoionization of Ca$^+$ is given schematically as

$$Ca^+ + h\nu \rightarrow Ca^{2+} + e, \qquad (1)$$
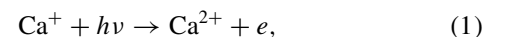
which is the direct photoionization pathway. In addition, however, the photoionization can proceed through an intermediate resonance; this pathway is represented as

$$Ca^+ + h\nu \rightarrow (Ca^+)^* \rightarrow Ca^{2+} + e. \qquad (2)$$
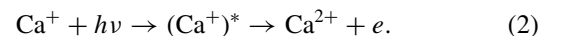
For the Ca$^+$ ions, the initial states considered, in the nonrelativistic photoionization calculations, are both the ground [Ne]$3s^23p^64s\,^2S^e$ state and the excited (metastable) [Ne]$3s^23p^63d\,^2D^e$ state, while in the relativistic calculations the initial states are the ground state [Ne]$3s^23p^64s\,^2S^e_{1/2}$ plus the first two excited (metastable) states, [Ne]$3s^23p^63d\,^2D^e_{3/2}$ and [Ne]$3s^23p^63d\,^2D^e_{5/2}$. The states of the final state ion Ca^{2+} are known in R-matrix language as the target states, with $N = 18$ electrons; those target ions are combined with the free electron to form the total final state, a $N + 1 = 19$ electron system. By dipole selection rules, the total final state (target state + unbound electron) can have (nonrelativistic symmetries) $^2P^o$, $^2D^o$, and $^2F^o$, i.e., the nonrelativistic allowed

———
[*]Present address: Department of Physics, Clark Atlanta University, Atlanta, GA 30314, USA.

transitions are given by

$$
\begin{aligned}
{}^2S^e + h\nu &\rightarrow {}^2P^o, \\
{}^2D^e + h\nu &\rightarrow {}^2P^o, {}^2D^o, {}^2F^o.
\end{aligned}
\tag{3}
$$

In the relativistic case, transitions (3) become

$$
\begin{aligned}
{}^2S^e_{1/2} + h\nu &\rightarrow {}^2P^o_{1/2}, {}^2P^o_{3/2}, \\
{}^2D^e_{3/2} + h\nu &\rightarrow {}^2P^o_{1/2}, {}^2P^o_{3/2}, {}^2D^o_{3/2}, {}^2D^o_{5/2}, {}^2F^o_{5/2}, \\
{}^2D^e_{5/2} + h\nu &\rightarrow {}^2P^o_{3/2}, {}^2D^o_{3/2}, {}^2D^o_{5/2}, {}^2F^o_{5/2}, {}^2F^o_{7/2}.
\end{aligned}
\tag{4}
$$

The target-state (Ca^{2+}) orbitals, in the present work, are obtained using the program AUTOSTRUCTURE [17–20]; the target-state wave functions and their energy levels are determined from configuration-interaction (CI) calculations using these orbitals. The nonrelativistic (LS-coupling scheme) and the relativistic (Breit-Pauli) R-matrix methods [20–26] are employed to carry out the photoionization cross-section calculations, and resonances in the region of giant $3p \rightarrow 3d$ excitations are analyzed (position, width, and identification) using the QB code [27–29]; the results of this resonance analysis are compared with available experimental and previous theoretical data [4,10,15].

II. THEORY AND METHOD OF CALCULATION

As mentioned above, the photoionization calculations were performed within the framework of the R-matrix methodology which was felt to be the most appropriate for this work for a variety of reasons. First, the existence of both relativistic and nonrelativistic versions allows us the opportunity to spotlight relativistic effects by performing the calculations both ways. Second, since R matrix is a "partitioned-space" theory, it allows us to include a great deal of correlation in the wave functions in the inner region (where correlation is most important) and omit correlation in the outer region, thereby allowing the inclusion of the important aspects of correlation while keeping the calculation tractable. Third, R matrix is equally applicable to atomic and ionic systems of any structure and symmetry, including both ground and excited states, unlike, say, the relativistic random phase approximation, which is only applicable to closed-shell systems. Fourth, in R matrix, resonances are built automatically into the photoionization cross section through the behavior of the final-state wave function whose description allows both routes, Eqs. (1) and (2), to be represented. This means, in practice, the final-state wave function contains both the open channels into which the resonance decays and the closed channels corresponding to the appropriate Rydberg series or resonance [30]. Finally, R matrix is flexible in that it allows the size of basis sets and the number of interacting channels to be varied. Thus, by increasing the size of these sets in increments, insight is gained as to which are the most important terms, and how convergence is approached.

To consider the photoionization of a $N+1$ electron system within an R-matrix framework, we start with the wave functions of the states of the N-electron final-state Ca^{2+} system, constructed by introducing a set of (target) states, and possibly pseudostates Φ_i that are usually written as a configuration-interaction (CI) expansion in terms of some

basis configuration functions ϕ_i:

$$
\Phi_i(x_1, x_2, \ldots, x_N) = \sum_k b_{ik}\phi_k(x_1, x_2, \ldots, x_N),
\tag{5}
$$

where $x_j = r_j\sigma_j$ represents the spatial and spin coordinates of the jth electron, and the b_{ik} are the ϕ_i configuration mixing coefficients. The configuration functions ϕ_i are constructed from a bound orbital basis set consisting of self-consistent field (SCF) orbitals plus some additional pseudo-orbitals included to model electron correlation effects. For a given ϕ_i configuration function, each one-electron orbital is a product of a radial function, a spherical harmonic, and a spin function. The discrete target states (Ca^{2+} ions) orbitals were generated using the code AUTOSTRUCTURE [17–20]. Each of the single-particle spectroscopic orbitals ($1s$, $2s$, $2p$, $3s$, $3p$, $3d$, $4s$, $4p$) and the pseudo-orbitals ($4\bar{d}$, $4\bar{f}$, $5\bar{s}$, $5\bar{p}$, $5\bar{d}$) radial wave functions were in the form of the Thomas-Fermi statistical model radial functions calculated within the program. The $1s$, $2s$, $2p$, $3s$, and $3p$ orbitals were optimized on the Ar-like ground state of Ca^{2+}. The $3d$ and $4s$ orbitals were optimized on a configuration-interaction (CI) calculation of the ${}^3P^o$ excited states on Ca^{2+} including $3s^23p^53d$, $3s^23p^54s$, and other configurations, and the $4p$ similarly with a CI on the excited ${}^3D^e$ state. All of the pseudo-orbitals were optimized on the ${}^3P^o$ excited-state CI including configurations $3p^53d$, $3p^54s$, $3p^33d^3$, $3p^54d$, $3p^55s$, $3p^55d$, $3p^43d4f$, $3p^43d5p$, among others. Using these orbitals, a CI expansion of the target (Ca^{2+}) configuration functions to obtain the N-electron target-state wave function was performed. The set of configuration functions included four spectroscopic configurations, $3s^23p^6$, $3s^23p^53d$, $3s^23p^54s$, and $3s^23p^54p$ and correlation configurations that, to begin with, included all one- and two-electron replacements of the $n = 3$ orbitals of the ground state of Ca^{2+} ions. To make the subsequent photoionization calculation more tractable, correlation configurations with very small coefficients in the CI expansions were removed, leaving us with 26 correlation configurations. Specifically, the correlation configurations included are $3s3p^65d$, $3s^23p^54d$, $3s^23p^54f$, $3s^23p^55s$, $3s^23p^55p$, $3s^23p^55d$, $3s3p^63d$, $3s^23p^43d^2$, $3s^23p^43d4p$, $3s^23p^44s4p$, $3s^23p^43d5p$, $3s^23p^44s5p$, $3s^23p^44p5p$, $3s^23p^44p4d$, $3s^23p^43d4f$, $3s^23p^44s4f$, $3s^23p^44p4f$, $3s^23p^33d^3$, $3s^23p^33d^24s$, $3s^23p^34s4p^2$, $3s^23p^34p^3$, $3s3p^53d^2$, $3s3p^53d4s$, $3s3p^53d4p$, $3s3p^43d^3$, and $3s3p^64p$. Thus, a total of 30 configurations corresponding to 682 LS terms were included in the nonrelativistic calculation; for the relativistic (BP) calculation, the relativistic spin-orbit, Darwin, and mass correction terms were added to the Hamiltonian and the resulting CI yielded LSJ terms constructed from the LS terms.

To get some idea of the accuracy of the N-electron target-state energy levels, we compare our results to earlier theoretical works [31,32] and experimental (NIST) [33] energy levels in electron volts relative to the ground state of Ca^{2+}; as demonstrated in Table I; reasonable agreement with experiment is seen.

Two separate photoionization cross-section calculations were performed for Ca^+ ions. In the first, relativistic effects were neglected, and the calculation was carried out with the LS-coupling nonrelativistic R-matrix codes [20–26]. In

TABLE I. Calculated (this work, Refs. [31,32]) and experimental (NIST [33]) energy levels in eV for states of Ca III (Ca^{2+}) relative to the ground state of Ca^{2+}.

Ca III state	J	Present	Expt. [33]	Ref. [31]	Ref. [32]
$3s^23p^6\,^1S^e$	0	0.000	0.000	0.000	0.000
$3s^23p^53d\,^3P^o$	0	25.069	25.215	25.570	23.948
	1	25.137	25.274	25.637	24.007
	2	25.274	25.397	25.768	24.125
$3s^23p^53d\,^3F^o$	4	26.429	26.323	26.570	25.089
	3	26.563	26.456	26.711	25.213
	2	26.686	26.574	26.839	25.323
$3s^23p^53d\,^1D^o$	2	28.209	27.999	28.388	26.832
$3s^23p^53d\,^3D^o$	3	28.182	28.062	28.308	26.889
	1	28.315	28.198	28.480	27.012
	2	28.338	28.192	28.507	27.005
$3s^23p^53d\,^1F^o$	3	28.462	28.320	28.320	27.154
$3s^23p^54s\,^3P^o$	2	29.873	30.072	31.471	28.763
	1	30.081	30.243	31.662	28.930
	0	30.272	30.452	31.856	29.120
$3s^23p^54s\,^1P^o$	1	30.738	30.710	32.232	29.396
$3s^23p^53d\,^1P^o$	1	34.874	34.635	34.635	33.915

our R-matrix calculations, the final $(N + 1)$ electron system continuum wave function is expressed in the form

$$
\begin{aligned}
\psi_k&(x_1, x_2, \ldots, x_{N+1}) \\
&= A \sum_{ij} c_{ijk} \Phi_i(x_1, \ldots, x_N; \hat{r}_{N+1}\sigma_{N+1}) \frac{1}{r_{N+1}} u_{ij}(r_{N+1}) \\
&\quad + \sum_j d_{jk} \chi_j(x_1, \ldots, x_{N+1}),
\end{aligned}
\tag{6}
$$

where the x_i denote the spatial $\hat{r}_i$ and the spin σ_i coordinates of the ith electron, the Φ_i are the channel functions obtained by coupling the target state and the angular and spin functions of the continuum electron to form states of the same total angular momentum and parity (and total angular momentum, J, in the Breit-Pauli calculation), and A is the antisymmetrization operator, which takes account of the exchange effects between the target electrons and the free electron. The functions u_{ij} are the single-particle continuum wave functions of the unbound electron, and the χ_i represent the quadratically integrable (L^2) functions, formed from the bound orbitals and included to ensure completeness of the expansion of the total wave function. In the first sum of Eq. (6), only the terms arising from three spectroscopic configurations ($3s^23p^6$, $3s^23p^53d$, and $3s^23p^54s$) are included which abnegates the possibility of pseudoresonances; those three configurations give rise to nine LS terms corresponding to 17 LSJ levels (see Table I). In the (purely discrete) second sum, however, all of the terms from the 30 N-electron configurations, coupled to all of the single-particle orbitals, both spectroscopic and correlation, are included in the set of χ_i.

The initial-state wave function for the Ca$^+$ ions, in this case, was constructed from adding a single electron to the N-electron target states to include the main configuration, $3s^23p^63d$ or $3s^23p^64s$, along with all single-electron promotions of the $3s$, $3p$, and the outer shell ($3d$ or $4s$), along

TABLE II. Ca II (Ca$^+$) states threshold energies in eV compared to experiment (Ref. [33]).

State	Calculation	Experiment	Error (%)
$^2S^e$	11.9868	11.8717	0.96
$^2D^e$	10.1653	10.1755	0.10
$^2S^e_{1/2}$	11.9853	11.8717	0.95
$^2D^e_{3/2}$	10.1664	10.1793	0.12
$^2D^e_{5/2}$	10.1499	10.1718	0.21

with all double promotions of the type $3s^23p^5nln'l'$, and the important double promotions of the $3s^23p^43d2nl$ variety. Other possible two-electron promotions were omitted to insure that the ground state was not overcorrelated as compared to the target states, i.e., to balance the calculation. The terms arising from these states formed the basis of a large CI calculation to obtain the initial-state wave function. In Table II are presented the threshold energies of the two nonrelativistic states of Ca$^+$, the ground [Ne]$3s^23p^64s\,^2S^e$ state and the excited [Ne]$3s^23p^63d\,^2D^e$ metastable state, along with the corresponding three relativistic initial states, the ground state [Ne]$3s^23p^64s\,^2S^e_{1/2}$ plus the first two (metastable) excited states [Ne]$3s^23p^63d\,^2D^e_{3/2}$ and [Ne]$3s^23p^63d\,^2D^e_{5/2}$. Comparing our theoretical ionization potentials with experimental data [33], also shown in the table, it is evident that agreement between theory and experiment is rather good. In both LS and BP calculations, the R-matrix box radius was 30.0 a.u., and 34 basis orbitals were used to represent the continuum for each value of the angular momentum.

III. RESULTS AND DISCUSSION

In the nonrelativistic calculations for Ca$^+$ ions, the initial states of this ion are the ground [Ne]$3s^23p^64s\,^2S^e$ and the excited (metastable) [Ne]$3s^23p^63d\,^2D^e$ states. In Fig. 1, we present results of the nonrelativistic calculations for photon energy from 23.0 to 46.0 eV. Figures 1(a) and 1(b) respectively illustrate the individual photoionization cross sections from ground $^2S^e$ and excited $^2D^e$ states of Ca$^+$; since, in both cases, the photoionization cross sections obtained using length and velocity forms agree very well, only one form (length) is displayed here and in all subsequent figures.

In the case of the Ca$^+$ ground $^2S^e$ state, the $4s$ threshold cross-section [not seen in Fig. 1(a)] magnitude is 0.1 Mb. For photon energy below 27.0 eV [Fig. 1(a)], there are no resonances in the ground $^2S^e$ state photoionization cross section; only the direct photoionization process is possible here, and leads to [$(3s^23p^6\,^1S^e)\,\varepsilon p$] $^2P^o$. Starting at 27.0 eV, we enter the $3p$ electron excitation region characterized by the presence of series of Rydberg resonances associated with $3p$ electron photoexcitation [Fig. 1(a)] such as [$(3p^5nd)\,4s\,^2P^o$] and [$(3p^5n's)\,4s\,^2P^o$]. These two sequences of Rydberg resonances contain the most important features of the Ca$^+$ ground $^2S^e$ state photoionization cross-section spectrum [Fig. 1(a)]; among them, we note the resonance located at 28.31 eV (2.1 meV width), and attributed to the transition $^2S^e \rightarrow 3p^5(4s^2\,^1S)\,^2P^o$ and the largest and broadest resonance feature in Fig. 1(a) at 33.18 eV (68.8 meV width); this last peak reaches 2200 Mb, and is attributed to the $^2S^e \rightarrow (3p^53d\,^1P)4s\,^2P^o$ transition
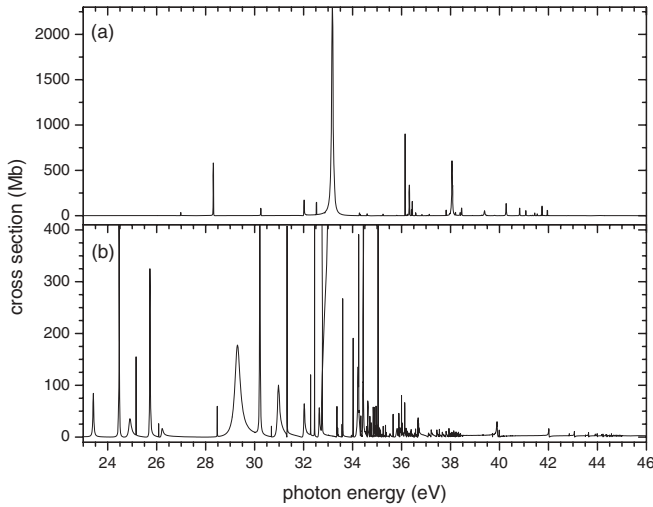
FIG. 1. Calculated nonrelativistic photoionization cross sections of Ca$^+$ from 23.0 to 46.0 eV: (a) initial $^2S^e$ ground state showing the strongest resonance $^2S^e \rightarrow (3p^53d~^1P)4s~^2P^o$ at energy 33.18 eV and (b) initial $^2D^e$ excited (metastable) state showing the strongest resonance $^2D^e \rightarrow 3p^5(3d^2~^3F)~^2F^o$ at energy 29.20 eV. Note the complexity of $^2D^e$ excited-state resonance structure compared to $^2S^e$ ground-state photoionization cross section.

that is followed by autoionization (decay) to the ground $3s^23p^6~^1S^e$ state of Ca^{2+}. Figure 1(a) also displays higher-order members of those Rydberg series of resonances originating from $3p$ electron photoexcitation to higher principal quantum number $[(3p^5nd)~4s~^2P^o]$ and $[(3p^5n's)~4s~^2P^o]$ with $n \geqslant 4$ and $n' \geqslant 5$, and they are mixed with, and interfere with, the underlying $[(3s^23p^6~^1S^e)~\varepsilon p~^2P^o]$ continuum. The limit of those two sequences is the excited target Ca^{2+} $(3p^54s~^1P^o)$ state at energy 42.58 eV (42.47 eV from experiment [33]). Due to dipole transition selection rules, only the transition $^2S^e \rightarrow ^2P^o$ is allowed; the limited number of resonances observed in this case [Fig. 1(a)] is illustrative of this fact.

For the excited (metastable) $^2D^e$ state of Ca$^+$, the photoionization cross section shown in Fig. 1(b) exhibits far more complex structure than the ground $^2S^e$ state of Ca$^+$. At threshold (10.16 eV in this work and 10.17 eV from experiment [33]), the cross section is 5.0 Mb [not shown in Fig. 1(b)], and up to photon energy 23.0 eV there are no resonances in the cross section; only the direct photoionization process occurs here, and leads to $[3s^23p^6~^1S^e~(\varepsilon f, \varepsilon p)~^2P^o, ^2F^o]$. For photon energy from 23.0 to 33.0 eV, we have a mixture of direct nonresonant and indirect resonance processes, and it is evident that the resonance excitations are dominant in this region where the cross section can reach hundreds of megabarns. Previous experimental and theoretical studies [11,12,14,15] of Ca$^+$ photoionization have shown that most of the significant contribution to the oscillator strength originated from this region, and the present theoretical results confirm this observation. In this energy region [Fig. 1(b)], we observe giant, $3p \rightarrow 3d$ excitation, resonances; they are strong because they represent $\Delta n = 0$ transitions, and, since the spatial extent of a wave function is determined largely by the principal quantum number, n, the $3p$ and $3d$ wave functions occupy substantially the same region of space, resulting in significant overlap and a

rather large dipole matrix element. The photoionization cross section in this region is dominated by resonances which decay via autoionizing processes leading to the ground $3s^23p^6~^1S^e$ state of Ca^{2+}. In this region, the direct photoionization contribution to the cross section is almost negligible in terms of the magnitude of the cross section, although the interference with the resonant channel in the wings of the resonances causes the line shapes of those giant resonances to be asymmetric, depending on the relative matrix elements of the two pathways (direct and indirect processes).

The most prominent features in this region of Fig. 1(b) include two types of resonances corresponding to the two allowed transitions in the case of the excited (metastable) $^2D^e$ state of Ca$^+$: $^2D^e \rightarrow ^2F^o$ and $^2D^e \rightarrow ^2P^o$ with $\Delta L = +1$ and $\Delta L = -1$, respectively. For the transition $^2D^e \rightarrow ^2P^o$, we observe, in Fig. 1(b), the resonance located at 23.41 eV (41.4 meV width) that is attributed to transition $^2D^e \rightarrow (3p^53d~^3P)4s$ $^2P^o$ and the resonance located at 30.21 eV (11.4 meV width), and is attributed to transition $^2D^e \rightarrow 3p^5(3d^2~^3P)$ $^2P^o$. For the transition $^2D^e \rightarrow ^2F^o$, the following resonances are the most important: the $^2D^e \rightarrow 3p^5(3d^2~^1G)$ $^2F^o$ resonance located at 24.46 eV (16.6 meV width), the $^2D^e \rightarrow 3p^5(3d^2~^1D)$ $^2F^o$ resonance located at 24.89 eV (119.6 meV width), the $^2D^e \rightarrow (3p^53d~^3F)4s~^2F^o$ resonance located at 25.72 eV (22.5 meV width), the $^2D^e \rightarrow (3p^53d~^1F)4s~^2F^o$ resonance located at 26.21 eV (75.5 meV width), the $^2D^e \rightarrow (3p^53d~^3P)4d~^2F^o$ resonance located at 30.96 eV (103.6 meV width), the $^2D^e \rightarrow (3p^53d~^3D)4d~^2F^o$ resonance located at 31.32 eV (2.0 meV width), the $^2D^e \rightarrow (3p^53d~^3F)4d~^2F^o$ resonance located at 32.02 eV (46.3 meV width) and the $^2D^e \rightarrow (3p^53d~^1D)4d~^2F^o$ resonance located at 32.63 eV (38.5 meV width). The largest and the strongest $^2D^e \rightarrow ^2F^o$ resonance is the $^2D^e \rightarrow 3p^5(3d^2~^3F)~^2F^o$ resonance located [Fig. 1(b)] at 29.29 eV (257.7 meV width). In fact all those giant resonances listed above and seen in Fig. 1(b) are the lowest and strongest members of the Rydberg series associated with the $3p$ photoexcitation that start from photon energy 23.0 eV and continue to the higher-energy region [Fig. 1(b)] with higher principal quantum number. As examples of those series of Rydberg resonance, we have $[(3p^5nd)~3d~^2P^o, ^2F^o]$ and $[(3p^5n's~^3P^o)~3d^2P^o, ^2F^o]$ with $n \geqslant 3$ and $n' \geqslant 4$ in Fig. 1(b).

These series of Rydberg resonances interfere with direct photoionization continua $3s^23p^6~^1S^e~(\varepsilon f, \varepsilon p)$, and converge at photon energy 35.37 eV to the excited Ca^{2+} state $3s^23p^53d~^3P^o$ for the excited $^2D^e$ state photoionization, and the upper limit of both series is the excited target Ca^{2+} $(3p^53d^1P^o)$ state at energy 44.97 eV (44.71 eV from experiment [33]). For the excited $^2D^e$ state photoionization, in the region above 35.37 eV [Fig. 1(b)], the photon energy is high enough to produce, through resonance excitation followed by autoionization, both ground and excited states of Ca^{2+} including $3s^23p^6~^1S^e$, $3s^23p^53d~^3P^o$, $3s^23p^53d~^3F^o$, etc., i.e., ionization plus excitation; the continuum cross sections (direct process) comprise $3s^23p^6~^1S^e~(\varepsilon f, \varepsilon p)$, $3s^23p^53d~^3P^o~(\varepsilon d, \varepsilon s)$, $3s^23p^53d~^3F^o~(\varepsilon d, \varepsilon s)$, and so forth.

In Fig. 2 we present cross sections from the excited (metastable) $^2D^e$ state of Ca$^+$ corresponding to all three allowed symmetries in the nonrelativistic regime: $^2D^e \rightarrow ^2F^o$, $^2D^e \rightarrow ^2D^o$, and $^2D^e \rightarrow ^2P^o$ [Figs. 2(a), 2(b), and 2(c),
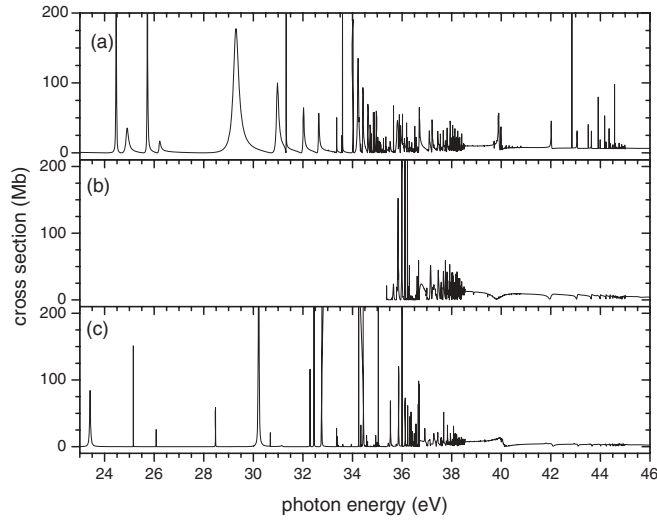
FIG. 2. Calculated nonrelativistic photoionization cross section for the Ca$^+$ excited (metastable) [Ne]$3s^23p^63d$ $^2D^e$ initial state for photon energy from 23.0 to 46.0 eV showing individual cross sections corresponding to all three allowed transitions from the $^2D^e$ initial state: (a) $^2D^e \rightarrow {}^2F^o$, (b) $^2D^e \rightarrow {}^2D^o$, and (c) $^2D^e \rightarrow {}^2P^o$. Note the transition $^2D^e \rightarrow {}^2D^o$ only occurs at photon energy above 35.37 eV, where the photon energy is high enough to produce both ground and excited states of Ca^{2+} including $3s^23p^6$ $^1S^e$, $3s^23p^53d$ $^3P^o$, $3s^23p^53d$ $^3F^o$, etc.

respectively] for photon energy from 23.0 to 46 eV. It is noteworthy that up to photon energy 35.37 eV, the Ca$^+$ photoionization cross section is only composed of the ejection of the $3d$ electron, leading to the ground state of the target Ca^{2+} $3s^23p^6$ $^1S^e$; consequently only two of those three symmetries ($^2D^e \rightarrow {}^2F^o$ and $^2D^e \rightarrow {}^2P^o$) are possible in this range of energy. However, for photon energy above 35.37 eV, all those three possibilities ($^2D^e \rightarrow {}^2F^o$, $^2D^e \rightarrow {}^2D^o$, and $^2D^e \rightarrow {}^2P^o$) are allowed, as seen in Fig. 2.

With the introduction of the spin-orbit interaction in our calculations through the use of the Breit-Pauli R-matrix method along with other relativistic effects, the initial states of the Ca$^+$ ion are characterized as the ground [Ne]$3s^23p^64s$ $^2S^e_{1/2}$ state, the first excited [Ne]$3s^23p^63d$ $^2D^e_{3/2}$ state, and the second excited [Ne]$3s^23p^63d$ $^2D^e_{5/2}$ state. The calculated relativistic (Breit-Pauli) cross sections for the photoionization of the Ca$^+$ $^2S^e_{1/2}$ initial state are shown in Fig. 3. The individual $^2S^e_{1/2} \rightarrow {}^2P^o_{3/2}$ and $^2S^e_{1/2} \rightarrow {}^2P^o_{1/2}$ cross sections are presented in Figs. 3(a) and 3(b), respectively, while the total is given in Fig. 3(c). As in the nonrelativistic case, the photoionization spectrum is dominated by autoionizing resonances, but now we distinguish two channels in the ground Ca$^+$ $^2S^e_{1/2}$ initial-state cross section: $^2S^e_{1/2} \rightarrow {}^2P^o_{3/2}$ and $^2S^e_{1/2} \rightarrow {}^2P^o_{1/2}$. Among the most important resonances in Fig. 3(a), which corresponds to transition $^2S^e_{1/2} \rightarrow {}^2P^o_{3/2}$, we note one large and strong resonance: the one located at 33.22 eV (72.2 meV width). Similarly from Fig. 3(b) for the $^2S^e_{1/2} \rightarrow {}^2P^o_{1/2}$ channel, we find the analogous resonance located at 33.20 eV (69.7 meV width). Other important resonance features in Figs. 3(a) and 3(b) are identified (position and width), and listed in Table III below.

FIG. 3. Calculated Breit-Pauli photoionization cross sections of the ground $^2S^e_{1/2}$ state of Ca$^+$ from 23.0 to 35.0 eV showing (a) the partial cross section to the $j = 3/2$ final state, (b) the partial cross section to the $j = 1/2$ final state, and (c) the total $^2S^e_{1/2}$ cross section, all dominated by the $^2S^e \rightarrow (3p^53d\,{}^1P)4s$ $^2P^o$ resonance at 33.22 eV. For simplicity $3p^5$ is omitted from each of the resonance designations.

Those two giant $3p \rightarrow 3d$ resonances in the $^2S^e_{1/2}$ cross sections' resonances (see above) are identified as $^2S^e_{1/2} \rightarrow (3p^53d\,{}^1P)4s$ $^2P^o_{3/2}$ in Fig. 3(a) and $^2S^e_{1/2} \rightarrow (3p^53d\,{}^1P)4s$ $^2P^o_{1/2}$ in Fig. 3(b); their positions and widths are 33.22 eV and 72.2 meV, and 33.20 eV and 69.7 meV, respectively. Although the relativistic interactions cause a splitting of these two resonances, the splitting is so much smaller than the widths that it is unobservable; thus they are equivalent to the single nonrelativistic resonance, $^2S^e \rightarrow (3p^53d\,{}^1P)4s$ $^2P^o$, and it was observed in the photoionization of excited [Ne]$3s^23p^64s$ $^2S^e_{1/2}$ state of Sc^{+2} [1,4,34–36]. From the present calculations, this giant resonance is located at 33.20 eV [Fig. 3(c)], and the experimental results [4,14,15] show it at 33.19 eV; i.e., there is excellent agreement between theory (this work) and experiment. We also note excellent agreement in the magnitude of this resonance which is about 2200 Mb both from experimental data [4,14,15] and theoretical calculations (this work); however, the width of this resonance is found (this work) to be 72.2 meV, which is smaller than the experimental width 91.0 meV [3,4,13–15], corresponding to 21% difference. In addition, this strong spectral line, $^2S^e \rightarrow (3p^53d\,{}^1P)4s$ $^2P^o$ transition, has a calculated oscillator strength (this work) of 1.87 out of a total of 6 ($3p$ photoexcitation); this is about 31.16% of the total oscillator strength, an important contribution. Here also we note discrepancies between the theoretical value (1.87 from this work) of this oscillator strength and the measured values that are 2.1 [4,6] or 2.2 [4,13]. Those differences between measured and calculated (this work) values of this specific oscillator strength (dipole-allowed $^2S^e \rightarrow (3p^53d\,{}^1P)4s$ $^2P^o$ transition) reveal how extremely difficult it is, even within the framework of the R-matrix method, to build accurate $(N + 1)$-electron system wave functions for such a complex atomic system (Ca$^+$ ions). Comparing the present calculated oscillator strengths to experimental results

TABLE III. Ca$^+$ resonance structures identification with resonance energies E_{res} (eV), widths Γ (meV), and corresponding transitions; experimental results [4,13–15] are shown where available.

Present			Experiment	
E_{res}	Γ	Transitions	E_{res}	Γ
26.95	2.1	$^2S_{1/2}^e \to 3p^5(3d^2\,^1D)\,^2P_{1/2}^o$		
27.00	1.7	$^2S_{1/2}^e \to 3p^5(3d^2\,^1D)\,^2P_{3/2}^o$		
28.57	1.8	$^2S_{1/2}^e \to 3p^5(4s^2\,^1S)\,^2P_{1/2}^o$	28.55	
28.20	2.3	$^2S_{1/2}^e \to 3p^5(4s^2\,^1S)\,^2P_{3/2}^o$	28.19	
30.45	5.3	$^2S_{1/2}^e \to 3p^5(3d^2\,^1S)\,^2P_{1/2}^o$	30.25	
30.17	5.6	$^2S_{1/2}^e \to 3p^5(3d^2\,^1S)\,^2P_{3/2}^o$	29.98	
32.02	12.3	$^2S_{1/2}^e \to 3p^5(3d^2\,^3P)\,^2P_{1/2}^o$		
32.07	10.9	$^2S_{1/2}^e \to 3p^5(3d^2\,^3P)\,^2P_{3/2}^o$		
33.21	69.7	$^2S_{1/2}^e \to (3p^53d\,^1P)4s\,^2P_{1/2}^o$	33.20	91.0
33.22	72.6	$^2S_{1/2}^e \to (3p^53d\,^1P)4s\,^2P_{3/2}^o$	33.20	91.0
23.33	42.3	$^2D_{3/2}^e \to (3p^53d\,^3P)4s\,^2P_{1/2}^o$		
23.44	40.9	$^2D_{5/2}^e \to (3p^53d\,^3P)4s\,^2P_{3/2}^o$		
23.46	40.9	$^2D_{3/2}^e \to (3p^53d\,^3P)4s\,^2P_{3/2}^o$		
25.14	2.1	$^2D_{3/2}^e \to 3p^5(3d^2\,^1D)\,^2P_{1/2}^o$		
25.19	1.7	$^2D_{5/2}^e \to 3p^5(3d^2\,^1D)\,^2P_{3/2}^o$		
25.20	1.7	$^2D_{3/2}^e \to 3p^5(3d^2\,^1D)\,^2P_{3/2}^o$		
28.67	5.3	$^2D_{3/2}^e \to 3p^5(3d^2\,^1S)\,^2P_{1/2}^o$		
28.37	5.6	$^2D_{5/2}^e \to 3p^5(3d^2\,^1S)\,^2P_{3/2}^o$		
28.39	5.6	$^2D_{3/2}^e \to 3p^5(3d^2\,^1S)\,^2P_{3/2}^o$		
30.20	12.3	$^2D_{3/2}^e \to 3p^5(3d^2\,^3P)\,^2P_{1/2}^o$	30.20	
30.23	10.9	$^2D_{5/2}^e \to 3p^5(3d^2\,^3P)\,^2P_{3/2}^o$	30.20	
30.24	10.9	$^2D_{3/2}^e \to 3p^5(3d^2\,^3P)\,^2P_{3/2}^o$	30.20	
30.78	0.2	$^2D_{3/2}^e \to (3p^53d\,^3P)4d\,^2P_{1/2}^o$		
30.95	0.2	$^2D_{5/2}^e \to (3p^53d\,^3P)4d\,^2P_{3/2}^o$		
30.97	0.2	$^2D_{3/2}^e \to (3p^53d\,^3P)4d\,^2P_{3/2}^o$		
32.26	3.2	$^2D_{3/2}^e \to (3p^53d\,^3F)4d\,^2P_{1/2}^o$		
32.52	2.3	$^2D_{3/2}^e \to (3p^53d\,^1P)4d\,^2P_{1/2}^o$		
32.42	3.4	$^2D_{5/2}^e \to (3p^53d\,^1P)4d\,^2P_{3/2}^o$		
32.44	3.4	$^2D_{3/2}^e \to (3p^53d\,^1P)4d\,^2P_{3/2}^o$		
32.86	3.9	$^2D_{3/2}^e \to (3p^53d\,^1D)4d\,^2P_{1/2}^o$		
24.55	14.2	$^2D_{3/2}^e \to 3p^5(3d^2\,^1G)\,^2F_{5/2}^o$		
24.53	14.2	$^2D_{5/2}^e \to 3p^5(3d^2\,^1G)\,^2F_{5/2}^o$		
24.37	15.4	$^2D_{5/2}^e \to 3p^5(3d^2\,^1G)\,^2F_{7/2}^o$		
24.77	17.7	$^2D_{5/2}^e \to 3p^5(3d^2\,^1D)\,^2D_{5/2}^o$		
24.76	17.7	$^2D_{3/2}^e \to 3p^5(3d^2\,^1D)\,^2D_{5/2}^o$		
24.85	119.6	$^2D_{3/2}^e \to 3p^5(3d^2\,^1D)\,^2F_{5/2}^o$		
24.84	119.6	$^2D_{5/2}^e \to 3p^5(3d^2\,^1D)\,^2F_{5/2}^o$		
24.94	125.1	$^2D_{5/2}^e \to 3p^5(3d^2\,^1D)\,^2F_{7/2}^o$		
25.74	22.5	$^2D_{3/2}^e \to (3p^53d\,^3F)4s\,^2F_{5/2}^o$		
25.72	22.5	$^2D_{5/2}^e \to (3p^53d\,^3F)4s\,^2F_{5/2}^o$		
25.70	30.7	$^2D_{5/2}^e \to (3p^53d\,^3F)4s\,^2F_{7/2}^o$		
25.78	6.1	$^2D_{3/2}^e \to (3p^53d\,^3D)4s\,^2F_{5/2}^o$		
25.76	6.1	$^2D_{5/2}^e \to (3p^53d\,^3D)4s\,^2F_{5/2}^o$		
26.39	75.3	$^2D_{3/2}^e \to (3p^53d\,^1F)4s\,^2F_{5/2}^o$		
26.02	57.8	$^2D_{5/2}^e \to (3p^53d\,^1F)4s\,^2F_{7/2}^o$		
26.37	75.3	$^2D_{5/2}^e \to (3p^53d\,^1F)4s\,^2F_{5/2}^o$		
26.17	17.6	$^2D_{5/2}^e \to (3p^53d\,^3D)4s\,^2F_{5/2}^o$		
29.25	251.6	$^2D_{3/2}^e \to 3p^5(3d^2\,^3F)\,^2F_{5/2}^o$	29.30	320.00
29.33	263.5	$^2D_{5/2}^e \to 3p^5(3d^2\,^3F)\,^2F_{7/2}^o$	29.30	320.00
29.24	251.6	$^2D_{5/2}^e \to 3p^5(3d^2\,^3F)\,^2F_{5/2}^o$	29.30	
30.09	0.5	$^2D_{3/2}^e \to 3p^5(3d^2\,^3F)\,^2D_{5/2}^o$	30.08	
30.08	4.2	$^2D_{3/2}^e \to 3p^5(3d^2\,^3F)\,^2D_{3/2}^o$	30.08	

TABLE III. *(Continued.)*

Present			Experiment	
E_{res}	Γ	Transitions	E_{res}	Γ
30.07	0.5	$^2D_{5/2}^e \to 3p^5(3d^2\,^3F)\,^2D_{5/2}^o$	30.07	
30.06	4.2	$^2D_{5/2}^e \to 3p^5(3d^2\,^3F)\,^2D_{3/2}^o$	30.07	
30.93	63.2	$^2D_{3/2}^e \to (3p^53d\,^3P)4d\,^2F_{5/2}^o$		
30.91	63.2	$^2D_{5/2}^e \to (3p^53d\,^3P)4d\,^2F_{5/2}^o$		
31.04	96.8	$^2D_{5/2}^e \to (3p^53d\,^3P)4d\,^2F_{7/2}^o$		
30.99	27.8	$^2D_{3/2}^e \to (3p^53d\,^3P)4d\,^2D_{5/2}^o$		
31.43	2.7	$^2D_{3/2}^e \to (3p^53d\,^3D)4d\,^2F_{5/2}^o$		
31.42	2.7	$^2D_{5/2}^e \to (3p^53d\,^3D)4d\,^2F_{5/2}^o$		
31.25	0.7	$^2D_{5/2}^e \to (3p^53d\,^3D)4d\,^2F_{7/2}^o$		
32.07	38.9	$^2D_{3/2}^e \to (3p^53d\,^3F)4d\,^2F_{5/2}^o$		
31.10	51.0	$^2D_{5/2}^e \to (3p^53d\,^3F)4d\,^2F_{7/2}^o$		
32.39	0.7	$^2D_{3/2}^e \to (3p^53d\,^1P)4d\,^2D_{5/2}^o$		
32.41	1.2	$^2D_{5/2}^e \to (3p^53d\,^1P)4d\,^2D_{3/2}^o$		
32.37	0.7	$^2D_{5/2}^e \to (3p^53d\,^1P)4d\,^2D_{5/2}^o$		
30.40	1.2	$^2D_{5/2}^e \to (3p^53d\,^1P)4d\,^2D_{3/2}^o$		
32.63	42.8	$^2D_{3/2}^e \to (3p^53d\,^1D)4d\,^2F_{5/2}^o$		
32.64	40.5	$^2D_{5/2}^e \to (3p^53d\,^1D)4d\,^2F_{7/2}^o$		
32.75	3.5	$^2D_{3/2}^e \to (3p^53d\,^1D)4d\,^2D_{3/2}^o$		
32.54	3.7	$^2D_{5/2}^e \to (3p^53d\,^1D)4d\,^2D_{5/2}^o$		

for the Ca$^+$ ions allows us to assess the quality of the $(N + 1)$-electron system wave functions.

The Breit-Pauli results for the photoionization of the excited (metastable) $^2D_{3/2}^e$ state of Ca$^+$ are presented in Fig. 4 for photon energy from 23.0 to 33.0 eV. From the excited $^2D_{3/2}^e$ state, transitions to final states with $j = 5/2$, $3/2$, and $1/2$ are allowed, and these cross sections are shown in Figs. 4(a)–4(c), respectively; the total $^2D_{3/2}^e$ photoionization cross section is
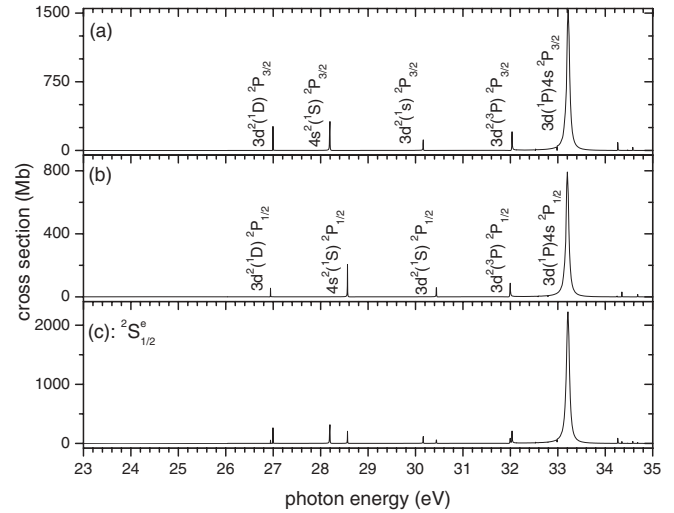

FIG. 4. Calculated Breit-Pauli photoionization cross sections of the ground $^2D_{3/2}^e$ state of Ca$^+$ showing (a) the partial cross section to the $j = 5/2$ final state, (b) the partial cross section to the $j = 3/2$ final state, (c) the partial cross section to the $j = 1/2$ final state, and (d) the total $^2D_{3/2}^e$ cross section, dominated by the $3p^5(3d^2\,^3F)\,^2F_{5/2}^o$ resonance at 29.25 eV. For simplicity $3p^5$ is omitted from each of the resonance designations.

shown in Fig. 4(d). For this entire photon energy range, resonances are seen to dominate the cross section, although the direct nonresonant photoionization channel is strong enough for interference to occur and produce the asymmetric line shapes, Fano profiles, observed in the cross sections [Figs. 4(a) and 4(d)]. The most prominent resonance is located at 29.25 eV with 251.6 meV width, and it is identified as $^2D^e_{3/2} \rightarrow 3p^5(3d^2\,^3F)\,^2F^o_{5/2}$, a $\Delta j = 1$ transition. This resonance decays via a super-Coster-Kronig [37,38] transition $(3p^53d^2 \rightarrow 3p^6 + e^-)$ that is also observed in the photoionization cross sections of the ground $[\mathrm{Ne}]3s^23p^63d\,^2D^e$ state of Sc^{+2} [1,3,4,34–36] and the ground $[\mathrm{Ne}]3s^23p^63d\,^2D^e$ state of Ti^{+3} [2–4,34–36,39–43]; as long as the excitation energy is above the $3d$ ionization threshold, this channel is open and results in this broad giant resonance.

When the excitation energy is below the $3d$ ionization threshold, this decay channel is closed, and this is the case for K-like higher-Z ions starting with V^{4+} (see [2,3]). Our theoretical results show good agreement with experimental data [4,14,15] that place this resonance at 29.33 eV (with 320.0 meV width). We note here that, compared to the $3d$ ionization threshold, the experimental positions of this resonance were [3,4,14,15] 19.16 eV in metastable Ca^+, 12.38 eV in ground state Sc^{2+}, and 0.22 eV in Ti^{3+}; our calculations (this work and [1,2]) show it at positions 19.17, 12.44, and 0.31 eV respectively. This result shows that we have reached good qualitative and quantitative agreement with experimental data [3,4] in reproducing this particularly strong and broad resonance feature whose position along the sequence get closer to the $3d$ ionization threshold as the nuclear charge Z increases. Besides this large resonance feature described above, many other important resonance structures exist in the case of excited (metastable) $^2D^e_{3/2}$ state of Ca^+. Those resonance structures are identified (position and width), and listed in Table III; they correspond to transitions with $\Delta j = +1$, 0, and -1 observed in Figs. 4(a)–4(c), respectively.

In Fig. 5 we present the calculated Breit-Pauli results for the corresponding photoionization cross section for the excited $^2D^e_{5/2}$ state of Ca^+ for photon energy from 23.0 to 33.0 eV, and the partial cross sections for $j = 7/2$, 5/2, and 3/2 final states are shown in Figs. 5(a)–5(c), respectively. The total photoionization cross section for the $^2D^e_{5/2}$ initial state is shown in Fig. 5(d). The strongest resonance, located at 29.33 eV in Figs. 5(a) and 5(d), and due to the $^2D^e_{5/2} \rightarrow 3p^5(3d^2\,^3F)$ $^2F^o_{7/2}$ transition, has a width of 263.5 meV (320.0 meV experimentally [3,14,15]); it is of substantially the same width as the corresponding $^2D^e_{3/2}$ resonance (with 251.6 meV width) at 29.25 eV [Figs. 4(a) and 4(d)]. Most resonances seen in Fig. 5 for the Ca^+ $^2D^e_{5/2}$ cross sections have their equivalent already listed in the case of Ca^+ $^2D^e_{3/2}$ (see Table III); among them are the transitions $^2D^e_{5/2} \rightarrow 3p^5(3d^2\,^3F)\,^2F^o_{5/2}$ seen at 29.24 eV (251.6 meV width) in Fig. 5(b) with $\Delta j = 0$ and $\Delta l = +1$, $^2D^e_{5/2} \rightarrow (3p^53d\,^3P)4s\,^2P^o_{3/2}$ ($\Delta j = -1$ and $\Delta l = -1$) located at 23.44 eV (40.9 meV width) in Fig. 5(c), and $^2D^e_{5/2} \rightarrow 3p^5(3d^2\,^3P)\,^2P^o_{3/2}$ seen at 30.23 eV (10.9 meV width) in Fig. 5(c). Another example of $\Delta j = 0$ but with $\Delta l = 0$ is seen in Fig. 5(b) at 30.07 eV (0.5 meV width), identified as $^2D^e_{5/2} \rightarrow 3p^5(3d^2\,^3F)\,^2D^e_{5/2}$. In addition there are also the $^2D^e_{5/2} \rightarrow (3p^53d\,^1F)4s\,^2F^o_{5/2}$, resonance at 26.37 eV (75.3 meV

FIG. 5. Calculated Breit-Pauli photoionization cross sections of the excited (metastable) $^2D^e_{5/2}$ state of Ca^+ showing (a) the partial cross section to the $j = 7/2$ final state, (b) the partial cross section to the $j = 5/2$ final state, (c) the partial cross section to the $j = 3/2$ final state, and (d) the total $^2D^e_{5/2}$ cross section, dominated by the $3p^5(3d^2\,^3F)\,^2F^o_{7/2}$ resonance at 29.33 eV. For simplicity $3p^5$ is omitted from each of the resonance designations.

width) in Fig. 5(b) and $^2D^e_{5/2} \rightarrow (3p^53d\,^1F)4s\,^2F^o_{7/2}$ at 26.13 eV (57.7 meV width), in Fig. 5(a).

The theoretical fine structure splitting between the $^2D^e_{3/2}$ and $^2D^e_{5/2}$ energy levels of Ca^+, which is $\Delta E = 0.016$ eV (experimental value is 0.008 eV [33]), is also mirrored between the following resonance energies: $^2D^e_{3/2} \rightarrow 3p^5(3d^2\,^3F)\,^2F^o_{5/2}$ at 29.254 eV in Fig. 4(a) and $^2D^e_{5/2} \rightarrow 3p^5(3d^2\,^3F)\,^2F^o_{5/2}$ at 29.238 eV in Fig. 5(b), $^2D^e_{3/2} \rightarrow (3p^53d\,^3P)4s\,^2P^o_{3/2}$ at 23.457 eV in Fig. 4(b) and $^2D^e_{5/2} \rightarrow (3p^53d\,^3P)4s\,^2P^o_{3/2}$ at 25.441 eV in Fig. 5(c), and $^2D^e_{3/2} \rightarrow 3p^5(3d^2\,^3P)\,^2P^o_{3/2}$ at 30.243 eV in Fig. 4(b) and $^2D^e_{5/2} \rightarrow 3p^5(3d^2\,^3P)\,^2P^o_{3/2}$ at 30.226 eV in Fig. 5(c). A summary of positions, widths, and identifications of the major resonances obtained in the relativistic Breit-Pauli calculation is given in Table III along with available experimental data [4,13–15]. In general the agreement is quite good, especially for the position of $3p^53d^2$ resonances, but our calculated widths are, in general, smaller than those from experimental data [4,13–15]. Note that some of the resonances listed in Table III can be reached by more than one initial state in the experimental mixture, and three of them $[3p^5(3d^2\,^3P)\,^2P^o_{3/2}, 3p^5(3d^2\,^1S)\,^2P^o_{3/2},$ and $3p^5(3d^2\,^1D)\,^2P^o_{3/2}]$, can be excited from all three initial states; using the example of $3p^5(3d^2\,^3P)\,^2P^o_{3/2}$, we clearly can illustrate the previous observation by the following three transitions: $^2D^e_{5/2} \rightarrow 3p^5(3d^2\,^3P)$ $^2P^o_{3/2}$ at 30.226 eV in Fig. 5(c), $^2D^e_{3/2} \rightarrow 3p^5(3d^2\,^3P)\,^2P^o_{3/2}$ at 30.243 eV in Fig. 4(b), and $^2S^e_{1/2} \rightarrow 3p^5(3d^2\,^3P)\,^2P^o_{3/2}$ at 32.062 eV in Fig. 3(a). They are listed more than once for purposes of comparison with the experimental results, and they are listed at different photon energies simply because each of the three initial states has a different ionization energy so that differing photon energies are required from each of these initial states to excite a particular resonance, i.e., the difference in the
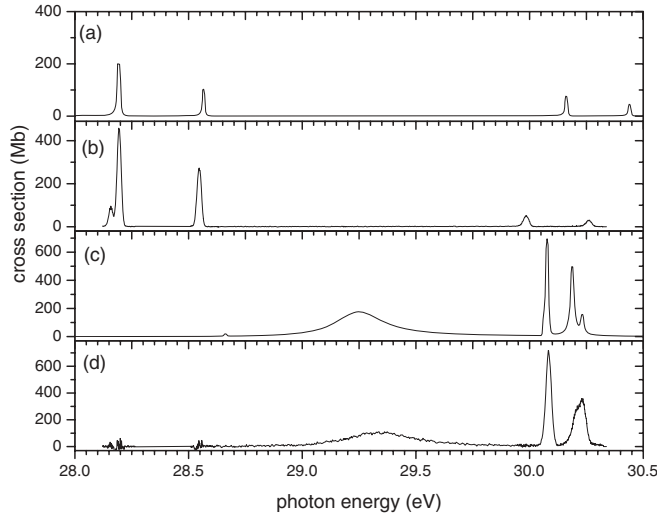
FIG. 6. Comparison of calculated (this work) Breit-Pauli photoionization cross sections and experimental measurements (Kjeldsen *et al.* [4,44]) for absolute photoionization cross sections for Ca$^+$ $3d$ and $4s$ ions showing (a) theoretical ground [Ne]$3s^2 3p^6 4s\,^2S^e$ state, (b) measured ground [Ne]$3s^2 3p^6 4s\,^2S^e$ state, (c) theoretical metastable [Ne]$3s^2 3p^6 3d\,^2D^e$ state, and (d) measured metastable [Ne]$3s^2 3p^6 3d\,^2D^e$.
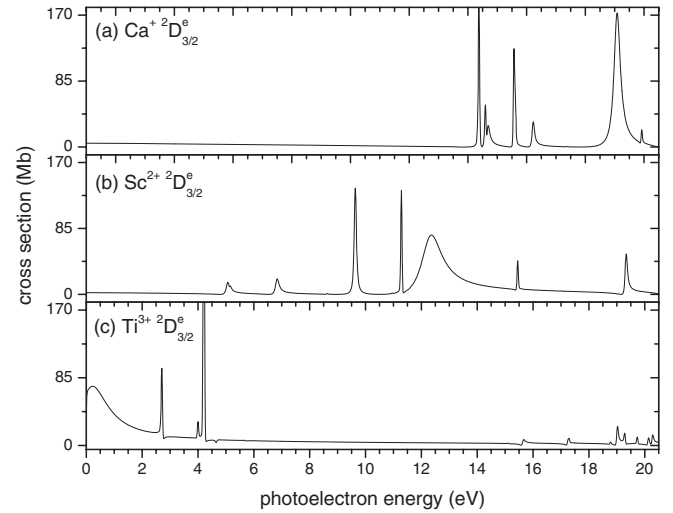

FIG. 7. Photoionization cross sections of potassiumlike ions in the $^2D^e_{3/2}$ state showing (a) excited-state Ca$^+$, (b) ground-state Sc^{++}, and (c) ground-state Ti^{3+}. Note, as we go from Ca$^+$ to Ti^{3+}, the strongest and largest resonance feature due to $^2D^e_{3/2} \rightarrow 3p^5(3d^2\,^3F)\,^2F^o_{5/2}$, the width increases, the magnitude decreases, and the position moves closer to the $3d$ ionization threshold.

resonance energies for a given resonance state in the table is just the difference in the binding energies of the initial states of the transitions.

The comparison of the present photoionization cross-section results with experimental data [44] is shown in Fig. 6 for Ca$^+$ in both the ground $4s$ and excited $3d$ states over the photon energy 28.0–30.5 eV; Figs. 6(a) and 6(b) represent cross sections for the Ca$^+$ ground [Ne]$3s^2 3p^6 4s\,^2S^e$ state while Figs. 6(c) and 6(d) are for the metastable Ca$^+$ [Ne]$3s^2 3p^6 3d\,^2D^e$ state. It is clear that, comparing Fig. 6(a) to Fig. 6(b) and comparing Fig. 6(c) to Fig. 6(d), relatively good agreement is reached with experimental results [4,14,15,44]. However, in Fig. 6, differences between theory and experiment in some of the resonance cross-section magnitudes are seen; as an illustration of this, the resonance structure due to $^2D^e \rightarrow 3p^5(3d^2\,^3P)\,^2P^o$ transition, located at 30.2 eV [Figs. 6(c) and 6(d)], is calculated (this work) to maximize at 550 Mb [Fig. 6(c)] while the experimental magnitude [4,44] is 275 Mb [Fig. 6(d)]. We note, however, the agreement between our calculated resonance positions and the experimental positions (Fig. 6) is excellent, and most of our cross-section magnitudes seen in Fig. 6 match their experimental counterparts observed in the same Fig. 6, or are within the margin of error, which is 15% for the experimental results depicted here [4,44].

It is of interest to explore the evolution of the very strong resonance structures due to giant $3p \rightarrow 3d$ dipole transitions followed by autoionization to continuum states (super-Coster-Kronig processes) exhibited for some members of the potassium isoelectronic sequence such as Ca$^+$, Sc^{2+}, and Ti^{3+} [1–4]. Looking at these three K-like ions (Ca$^+$, Sc^{2+}, and Ti^{3+}), we consider the $3d$ sequence which is described with each of the two initial states [Ne]$3s^2 3p^6 3d\,^2D^e_{3/2}$ and [Ne]$3s^2 3p^6 3d\,^2D^e_{5/2}$; it includes the ground and first excited

states of Sc^{+2} and Ti^{+3} and the first two excited states of Ca$^+$. The $3d$ sequence comparison is shown in Fig. 7, and we focus particularly on the strongest resonance features in those cross sections, the $^2D^e_{3/2} \rightarrow 3p^5(3d^2\,^3F)\,^2F^o_{5/2}$ (Fig. 7) and $^2D^e_{5/2} \rightarrow 3p^5(3d^2\,^3F)\,^2F^o_{7/2}$ (not shown here). Figure 7(a) concerns Ca$^+$, Fig. 7(b) Sc^{2+}, and Fig. 7(c) Ti^{3+}, all for the $^2D^e_{3/2}$ initial state. In Fig. 7 we observe, as the nuclear charge Z increases from Ca$^+$ to Ti^{3+} ($Z = 20$ to $Z = 22$) the position of this particular resonance [$^2D^e_{3/2} \rightarrow 3p^5(3d^2\,^3F)\,^2F^o_{5/2}$ transition] moves closer to the ionization threshold; for higher-Z ($Z \geqslant 23$) members of the sequence, these giant resonances are located below the threshold and are, thus, purely discrete states. It is also seen from Fig. 7 that the width of the strongest resonance [$^2D^e_{3/2} \rightarrow 3p^5(3d^2\,^3F)\,^2F^o_{5/2}$ transition] increases from Ca$^+$ to Ti^{3+}. Very similar behavior is observed in the evolution of the resonance associated with the $^2D^e_{5/2} \rightarrow 3p^5(3d^2\,^3F)\,^2F^o_{7/2}$ transition for the [Ne]$3s^2 3p^6 3d\,^2D^e_{3/2}$ initial-state spectra from Ca$^+$ to Ti^{3+} (not shown).

IV. CONCLUDING REMARKS

We have performed nonrelativistic (LS-coupling) and relativistic (Breit-Pauli) photoionization cross-section calculations for ground and excited states of Ca$^+$ ions. Our theoretical results show good agreement with experimental data [4,14,15,44], especially in terms of the positions of major resonances. The Ca$^+$ photoionization cross-section spectra reveal the presence of giant $3p \rightarrow 3d$ resonances, the same strong resonance structures that were observed in K-like transition-metals ions [1–4] such as Sc^{2+} and Ti^{3+}, which indicated the desirability of a study of those strong resonance features along the isoelectronic sequence with the comparison

involving the $3d$ initial states. From this comparison, it was observed that the strongest and broadest resonance feature of each of those sequences evolved theoretically the same way as in experiment [3,4,13–16]; as the nuclear charge Z increases from Ca$^+$ to Ti^{+3}, the width increases, the magnitude decreases, and the position is closer to the ionization threshold, the $3d$ threshold.

For the photoionization cross-section calculations for Ca$^+$, we must point out that our calculated widths for resonances due to transitions $^2S^e \rightarrow (3p^53d\ ^1P)4s\ ^2P^o$, $^2D^e_{3/2} \rightarrow 3p^5(3d^2\ ^3F)$ $^2F^o_{5/2}$, and $^2D^e_{5/2} \rightarrow 3p^5(3d^2\ ^3F)\ ^2F^o_{7/2}$ are all smaller than their experimental counterparts [3,13–16], but this difference in widths represents the only significant discrepancies between the present theory and experiment; in terms of resonance positions, the present results and experimental data are in excellent agreement without any shift in our theoretical resonance positions.

[1] A. M. Sossah, H.-L. Zhou, and S. T. Manson, Phys. Rev. A **78**, 053405 (2008).

[2] A. M. Sossah, H.-L. Zhou, and S. T. Manson, Phys. Rev. A **82**, 043416 (2010).

[3] S. Schippers, A. Müller, R. A. Phaneuf, T. van Zoest, I. Álvarez, C. Cisneros, E. D. Emmons, M. F. Gharaibeh, G. Hinojosa, A. S. Schlachter, and S. W. J. Scully, J. Phys. B **37**, L209 (2004).

[4] H. Kjeldsen, J. Phys. B **39**, R325 (2006).

[5] B. Sonntag and P. Zimmerman, Rep. Prog. Phys. **55**, 911 (1992).

[6] J. E. Hansen, H. Kjeldsen, F. Folkmann, M. Martins, and J. B. West, J. Phys. B **40**, 293 (2007).

[7] J. B. West, Radiat. Phys. Chem. **70**, 275 (2004).

[8] M. W. D. Mansfield and G. H. Newson, Proc. R. Soc. London A **357**, 77 (1977).

[9] G. Miecznikt, K. A. Berrington, P. G. Burke, and A. Hibbert, J. Phys. B **23**, 3305 (1990).

[10] V. K. Ivanov and J. B. West, J. Phys. B **26**, 2099 (1993).

[11] J. E. Hansen and P. Quinet, J. Electron Spectrosc. **79**, 307 (1996).

[12] A. Hibbert and J. E. Hansen, J. Phys. B **32**, 4133 (1999).

[13] I. C. Lyon, B. Peart, K. Dolder, and J. B. West, J. Phys. B **20**, 1471 (1987).

[14] A. Müller, S. Schippers, A. M. Covington, A. Aguilar, G. Hinojosa, R. A. Phaneuf, M. M. Sant Anna, A. S. Schlachter, J. D. Bozek, and C. Cisneros, in *ICPEAC 2001: Abstracts of Contributed Papers* (Rinton, Princeton, NJ, 2001), p. 52.

[15] A. Müller, S. Schippers, A. M. Covington, A. Aguilar, G. Hinojosa, R. A. Phaneuf, M. M. Sant Anna, A. S. Schlachter, J. D. Bozek, and C. Cisneros, in *Photo-ionization of Potassium-like Ions: Spectroscopy of Autoionizing States*, [http://www.als.lbl.gov/als/compendium/AbstractManager/uploads/00040.pdf].

[16] H. Kjeldsen, F. Folkmann, F. Innocenti, L. Zuin, and J. E. Hansen, J. Phys. B **35**, L375 (2002).

[17] W. Eissner, M. Jones, and H. Nussbaumer, Comput. Phys. Commun. **8**, 270 (1974).

[18] N. R. Badnell, J. Phys. B **19**, 3827 (1986).

[19] N. R. Badnell, J. Phys. B **30**, 1 (1997).

[20] UK APAP Codes: [http://amdpp.phys.strath.ac.uk/tamoc/code.html].

[21] P. G. Burke and K. A. Berrington, *Atomic and Molecular Processes: An R-matrix Approach* (IOP Publishing, Bristol, UK, 1993).

[22] K. A. Berrington, W. B. Eissner, and P. H. Norrington, Comput. Phys. Commun. **92**, 290 (1995).

[23] K. A. Berrington, P. G. Burke, J. J. Chang, A. T. Chivers, W. D. Robb, and K. T. Taylor, Comput. Phys. Commun. **8**, 149 (1974).

[24] K. A. Berrington, P. G. Burke, M. Le Dourneuf, W. D. Robb, K. T. Taylor, and Vo Ky Lan, Comput. Phys. Commun. **14**, 367 (1978).

[25] P. G. Burke and W. D. Robb, in *Advances in Atomic and Molecular Physics* (Academic Press, New York, 1975), Vol. 11, pp. 143ff.

[26] P. G. Burke, C. J. Noble, and V. M. Burke, in *Advances in Atomic, Molecular and Optical Physics* (Academic Press, New York, 2007), Vol. 54, pp. 237ff.

[27] K. Berrington, L. Quigley, and J. Pelan, Comput. Phys. Commun. **114**, 225 (1998).

[28] L. Quigley and K. Berrington, J. Phys. B **29**, 4529 (1996).

[29] J. M. Ramirez and M. A. Bautista, J. Phys. B **35**, 4139 (2002).

[30] P. G. Burke, in *Atomic Processes and Applications*, edited by P. G. Burke and B. L. Moiseiwitsch (North-Holland, Amsterdam, 1976), Chap. 7, p. 199.

[31] D. Nikolić, T. W. Gorczyca, K. T. Korista, and N. R. Badnell, Astron. Astrophys. **516**, A97 (2010).

[32] C. Froese Fischer, G. Tachiev, and A. Irimia, At. Data Nucl. Data Tables **92**, 607 (2006).

[33] NIST: [http://physics.nist.gov/PhysRefData/ASD/levels_form.html].

[34] S. Schippers, A. Müller, S. Ricz, M. E. Bannister, G. H. Dunn, J. D. Bozek, A. S. Schlachter, G. Hinojosa, C. Cisneros, A. Aguilar, A. M. Covington, M. F. Gharaibeh, and R. A. Phaneuf, Phys. Rev. Lett. **89**, 193002 (2002).

[35] S. Schippers, A. Müller, S. Ricz, M. E. Bannister, G. H. Dunn, A. S. Schlachter, G. Hinojosa, C. Cisneros, A. Aguilar, A. M. Covington, M. F. Gharaibeh, and R. A. Phaneuf, Phys. Rev. A **67**, 032702 (2003).

[36] J. Zeng, G. Zhao, and J. Yuan, Phys. Rev. A **68**, 022714 (2003).

[37] R. E. Dietz, E. G. Mc Rae, Y. Yafet, and C. W. Caldwell, Phys. Rev. Lett. **33**, 1372 (1974).

[38] L. C. Davis and L. A. Feldkamp, Solid State Commun. **19**, 413 (1976).

[39] S. N. Tiwary, A. E. Kingston, and A. Hibbert, J. Phys. B **16**, 2457 (1983).

[40] T. W. Gorczyca, M. S. Pindzola, D. C. Griffin, and N. R. Badnell, J. Phys. B **27**, 2399 (1994).

[41] A. N. Ryabtsev, S. S. Churilov, and Ya. É. Kononov, Opt. Spectrosc. **98**, 519 (2005).

[42] D. Nikolić, T. W. Gorczyca, and N. R. Badnell, Phys. Rev. A **79**, 012703 (2009).

[43] W. Eissner, N. Huu Hoa, and L. Vo Ky, in *Calculations on Photoionization of Ti^{3+}*, [http://web.am.qub.ac.uk/apa/ICPEAC09/01-Photon%20Impact%20(Weak%20Field)/01-5-Photoionization%20of%20ions/Fr157.pdf].

[44] [http://www.phys.au.dk/~hkj/data.html].